

SUPPLEMENTARY INFORMATION for

Apparent Yield Stress, High Shear Rate Viscosity and Interfacial Viscoelasticity of Bovine Serum Albumin Solutions

Vivek Sharma¹, Aditya Jaishankar¹, Ying-Chih Wang², Gareth H. McKinley¹

¹Hatsopoulos Microfluids Laboratory, Department of Mechanical Engineering, Massachusetts Institute of Technology, Cambridge, MA 02139-4307.

²Rheosense Inc, San Ramon, CA”

In this document, we include additional details and supporting discussions for the principal experimental results presented in the main paper. We also provide a detailed derivation for the simple additive model that relates the shear-rate–dependent interfacial viscosity and Newtonian-like, shear-rate–independent viscosity, measured independently in the VROC, to the total apparent rate-dependent viscosity measured on the cone-and-plate (CP) and double gap (DG) geometries on a torsional rheometer.

RESULTS AND DISCUSSION

Bulk rheology and high shear viscometry

In the main text of the paper, we argued that the flow curves measured with the cone-and-plate (CP) geometry on a stress-controlled rheometer, provide a measure of the apparent viscosity data that contains a contribution from the interfacial BSA film formed on the free surface. In figure 1 of the paper, we showed how CP data and data from the double gap (DG) Couette geometry systematically deviate from each other, whereas the DG data measured at high shear rates agrees quite well with measurements performed on the interface-free microfluidic rheometer (VROC; Rheosense Inc., San Ramon, CA). We noted in the main text that the pressure drop, ΔP required to drive the flow with rate Q is related to the wall shear stress, τ_w by the expression $w d \Delta P = 2L(w + d)\tau_w$, whereas the nominal wall shear rate, $\dot{\gamma}_w$ associated with fully developed laminar flow of a Newtonian fluid is $\dot{\gamma}_w = 6Q/wd^2$. The specific microfluidic device used in this study, mVROC – Type A05 chipset, consists of a rectangular cross-section channel ($w = 3.02$ mm; $d = 50$ μ m) made out of Pyrex mounted on a gold-coated silicon base containing three flush mounted pressure sensors. In a typical experiment, the shear rate is varied

by varying the flow rate, Q using a syringe pump and 2.5 mL Hamilton Gastight glass syringes (Reno, NV, USA). The VROC device outputs the pressure drop as a function of flow rate and the data can then be used to determine the nominal or apparent viscosity $\eta(\dot{\gamma}) = \tau_w / \dot{\gamma}_w$. The pressure measured by each of the three sensors as a function of sensor location along the channel is shown in Figure SI.1a for different shear rates for the representative case of a 50 mg/ml BSA solution. The pressure drop per unit length between the sensors is a constant for each shear rate. Furthermore, the raw data for pressure drop vs flow rate (or ΔP vs Q) data presented in figure SI.1b shows that the measured pressure drop between sensors increases linearly with increase in the flow rate for all concentration of BSA studied, as is typical for Newtonian fluids.

Figure SI.1

To ensure that the measured values in the microfluidic channel are repeatable and accurate, we present (in the main text) tests carried out with a Newtonian calibration oil (see figure 3 in main text). The difference between a Newtonian fluid and the apparent shear thinning displayed by the BSA solutions is easily visible. In addition, we carried out an internal check of our data by probing the shear viscosity behavior of BSA solutions independently in two laboratories using different microfluidic rheometers. Figure SI.2 shows the comparison of VROC measurements performed at two locations, firstly at the research lab at MIT and, secondly, independent measurements at Rheosense Inc., San Ramon, CA. We find good agreement (to within 5 %) between the two data sets over the concentration range $10 \leq c \leq 200$ mg/ml, and this (along with arguments presented in main text) emphasizes the fact that the viscosity response of BSA solutions in a interface-free geometry shows no shear thinning.

Figure SI.2

Interfacial viscosity and viscoelasticity

Master curves for the storage and loss components of the interfacial viscoelastic modulus measured in oscillatory strain sweep experiments at a fixed frequency of $\omega = 1$ rads^{-1} , were plotted in Figure 4 in the main paper by shifting all of the measured the data to a reference concentration of 50 mg/ml. In Figure SI.3, we show the unshifted, raw data for the storage and loss moduli for the different concentrations of BSA used. We have also included a schematic

diagram of the DWR fixture. It is clear that both the elastic and viscous components of the complex modulus $G^*(\omega)$ increase with concentration. The sudden downturn in both the storage and loss modulus at a strain amplitude of about 1% indicates the onset of yielding in the interfacial film. We have already noted in the main text that the measured interfacial elasticity falls rapidly beyond this critical yield strain, $\gamma_Y \approx 0.01$, and therefore the nominal interfacial tension required to break the interfacial structure of the adsorbed BSA (or cause yielding of interfacial layer) is of the order of $\tau_{sY} = G'_s \gamma_Y \approx 10^{-4}$ Pa.m. It is worth noting that this value is close to the interfacial tension measured in steady shear, $\tau_{sY} = \eta_s \dot{\gamma} \approx 10^{-4}$ Pa.m at the lowest imposed shear rates (10^{-2} s^{-1}) presented in Figure SI.4.

Figure SI.3

The universal yielding behavior of the interfacial film can be illustrated more clearly by plotting mastercurves of the total interfacial stress, $a(c)\tau_s = |G_s^*(c)|\gamma_0$ or the elastic contribution $a(c)\tau_s = G'_s(c)\gamma_0$ (where $a(c)$ represents the shift factor for each concentration of BSA), measured in interfacial oscillatory shear experiments against the applied strain, $\gamma_0/b(c)$, as shown in Figure SI.4. The magnitude of the interfacial stress τ_s initially increases linearly with increase in the applied strain amplitude but, beyond a critical strain value, the elastic contribution of the stress passes through a maximum implying that the interface yields and begins to flow plastically, as shown by the plateau in the total stress amplitude observed at higher strain values in Figure SI.4.

Figure SI.4

Extracting interfacial viscosity contribution from bulk viscosity

The simple physical arguments and equations 5-7 presented in the main text of the paper can be used to make *a priori* estimates of the interfacial viscosity η_s for the BSA rich interfaces based on the knowledge of the apparent bulk viscosity η_B measured with test fixtures on a torsional rheometer (with a solution/air interface), and independent measurements of the high shear rate viscosity η_∞ (measured in a device such as the VROC, in which there is no interface present). The appropriate derivation for the DG geometry was outlined in the paper, and the corresponding relations for the CP and the DG geometry are derived in more detail here.

We begin with Equation 5 in the paper, which we write here again for clarity. The torque measured by a rheometer using the double gap geometry is given by adding the contributions from the subphase and the interface (sketched in figure SI.5) as follows:

$$M^{DG}(\dot{\gamma}) = 2 \left[2\pi R(L - \delta)\tau_B + 2\pi R\delta \left(\frac{\tau_s}{\delta} \right) \right] R \quad (\text{SI.1})$$

All variables here are as defined in the main text, and L and R are specifically the length and the radius of the rotating Couette cylinder as sketched in Figure SI.5. The interfacial contribution to the total shear stress is defined as a force per unit length (i.e. it has units of a surface tension) and arises physically from the surface enrichment (or “surface excess”) in the concentration of BSA. In the simplest description, this interfacial viscous tension provides an additional contribution to the torque of magnitude $2 \times (2\pi R\tau_s) \times R$, implying that the corresponding shear stress for an idealized adsorbed layer of thickness δ is τ_s / δ . The sketch also shows that the adsorption leads to a concentration gradient near the interface, and the absolute value of the prefactor A might change with the protein solution and interface being investigated. But we will simply consider an idealized case where the layer thickness is δ .

Equivalently the macroscopic apparent viscosity measured by the controlled stress rheometer is

$$\eta(\dot{\gamma}) \equiv \frac{M^{DG}}{4\pi R^2 L \dot{\gamma}} = \frac{1}{\dot{\gamma}} \left[\left(1 - \frac{\delta}{L} \right) \tau_B + \left(\frac{\tau_s}{L} \right) \right] \quad (\text{SI.2})$$

Provided $\delta \ll L$, this expression can be combined with the definitions $\tau_B = \eta_\infty \dot{\gamma}$ and $\tau_s = \eta_s(\dot{\gamma}) \dot{\gamma}$ for the rate-independent bulk and rate-independent surface contributions to the stress respectively to give the following result (compare with equation 6 in the main text)

$$\eta^{DG}(\dot{\gamma}) \equiv \eta_\infty + \frac{\eta_s(\dot{\gamma})}{L} \quad (\text{SI.3})$$

We use this expression to make an estimate of $\eta(\dot{\gamma})$ from the independent measurements of $\eta_s(\dot{\gamma})$ and η_∞ , and the resulting bulk viscosity is shown by the dotted line in figure SI.6. The

estimated value compares quite well with the response measured with the DG geometry (symbols) over a wide range of shear rates.

Figure SI.6

We note that this simple calculation neglects any coupling between the shearing flow of the viscous interface and the lower-viscosity subphase. As the viscoelastic interface essentially rides on the flow generated in the subphase in double gap geometry, its contribution to the total stress is less than what it would be in the pure shearing case with no subphase flow. Precise calculation of this coupling requires solution of the full hydrodynamics problem (see for example Vandebril et al ¹) and varies with the Boussinesq number characterizing the interface. Thus, while the measurement using DG geometry might manifest some effects of an interfacial layer, the interfacial viscosity will be measured to a higher accuracy by a geometry where the deformation is localized to the interface.

Figure SI.6

In contrast to measurements with the DG geometry, the total torque measured in the DWR geometry is primarily from the response to the deformation applied to the interface because of the much larger value of the wetted perimeter ($l^{DWR} = A / P \approx 0.7 \text{ mm}$), though it still includes a small contribution from dissipation that occurs from the weak flow established in the bulk (described in Vandebril et al ¹ for the DWR geometry). Detailed calculations show that provided $Bo_s \gg 1$ the bulk flow is negligible. For the DWR measurements with BSA solutions presented in this work, we find $68 \leq Bo_s \leq 58640$ and we can safely ignore coupling for the experiments performed with the DWR fixture.

If we again assume an additive contribution from the bulk and interfacial stresses then the corresponding expression for the torque in a cone-and-plate (CP) fixture is

$$M^{CP}(\dot{\gamma}) = \int_0^{R-\delta} r \tau_B 2\pi r \, dr + \int_{R-\delta}^R \frac{\tau_s}{\delta} 2\pi r \, r dr \quad (\text{SI.4})$$

The apparent viscosity measured by the rheometer is then given by performing the integrations in Equation SI.4 and making the approximation that $\delta \ll R$. The resulting expression is

$$\eta(\dot{\gamma}) \equiv \frac{M^{CP}(\dot{\gamma})}{(2\pi R^3 / 3)\dot{\gamma}} = \eta_\infty + \frac{3\eta_s(\dot{\gamma})}{R} \quad (\text{SI.5})$$

Where again we have substituted the measured rate-independent bulk viscosity $\tau_B = \eta_\infty \dot{\gamma}$ and the rate-independent surface contribution $\tau_s = \eta_s(\dot{\gamma}) \dot{\gamma}$.

In summary, the apparent viscosity of a surface active complex fluid such as an albumin solution measured by a standard torsional rheometer can be written quite generally in the form

$$\eta(\dot{\gamma}) = \eta_\infty + l_G^{-1} \eta_s(\dot{\gamma}) \quad (\text{SI.6})$$

Where l_G is a characteristic length scale for the geometry of interest. For the cone-and-plate geometry, we find $l_G^{(CP)} = R/3$ and for the double gap couette cell $l_G^{(DG)} = L$. Or equivalently in dimensionless form,

$$\frac{\eta(\dot{\gamma})}{\eta_\infty} = 1 + \frac{\eta_s(\dot{\gamma})}{l_G \eta_\infty} = 1 + Bo_s(\dot{\gamma}) \quad (\text{SI.7})$$

where $Bo_s(\dot{\gamma})$ is a rate-dependent Boussinesq number. The resulting bulk viscosity $\eta(\dot{\gamma})$, estimated using equations SI.3-SI.7, using independent measurements of $\eta_s(\dot{\gamma})$ and η_∞ shown by the dotted line in figure SI.6, compares quite well with the measured values (symbols).

In the experiments shown in Figures 1 and 3 and SI.1, the Boussinesq number for the concentration $c = 100$ mg/ml using the DG geometry decreases from values as large as $Bo_s^{(DG)} = 690$ at $\dot{\gamma} = 1 \text{ s}^{-1}$ (corresponding to complete dominance of interfacial effects) down to $Bo_s^{(DG)} = 0.8$ at $\dot{\gamma} = 10^3 \text{ s}^{-1}$ at which point the bulk viscous stresses begin to dominate the total measured response. Figure SI.7 shows the variation in the Boussinesq numbers for the different geometries used in the present study as a function of shear rate.

Figure SI.7

The apparent shear thinning behavior observed from torsional rheometer tests with globular protein solutions is thus a consequence of the additive effect from these two contributions, with the rate-dependent interfacial contribution leading to the observed shear thinning. We have indicated in the main text that equation SI.6 can be simplified even further if the interfacial stress is modeled as a perfect plastic with a yield stress τ_{sY} . In this case, the apparent viscosity expression SI.6 becomes of Bingham-like form

$$\eta(\dot{\gamma}) \approx \eta_{\infty} + \frac{1}{l_G} \frac{\tau_{sY}}{\dot{\gamma}} \quad (\text{SI.8})$$

The entire measured flow curve can thus be described in terms of two material properties τ_{sY} , η_{∞} and a single characteristic geometric scale l_G . Similarly we have pointed out in the main text that if a DWR fixture is not available for directly measuring the interfacial viscosity, then an independent estimate can likewise be made from the measurement of apparent bulk viscosity on a torsional rheometer and independent measurement of the interface-free response in the microfluidic rheometer. Rearranging equation SI.6 gives

$$\eta_s(\dot{\gamma}) \equiv l_G (\eta(\dot{\gamma}) - \eta_{\infty}) \quad (\text{SI.9})$$

With the values for the characteristic length scales for the different geometries used being the same as given above near Equation SI.7. This estimate of $\eta_s(\dot{\gamma})$ is shown by the dashed line of figure SI.7 (Figure 7 of the main text). As mentioned earlier the lower estimate of $\eta_s(\dot{\gamma})$ from this simple calculation neglects the fact that as the viscoelastic interface essentially rides on the flow generated in the subphase of the DWR geometry when mounted on a torsional rheometer, its contribution to the total stress is less than what it would be in the pure shearing case with no subphase flow,

We also mention here that the concept of a yield stress, the problems associated with measuring an accurate value for this viscoplastic material property and its utility in describing behavior of soft materials including biofluids like blood are discussed in detail in a review by Barnes ². While serum albumins are important constituents of blood, the yield stress in blood arises primarily from the presence of red blood cells ³⁻⁵, and in blood rheology the effect of serum albumins is primarily in raising the viscosity of the background fluid plasma ⁵. The yield stress data measured for human blood samples lies in the range $\tau_Y \approx 10^{-4} - 10^{-1}$ Pa; the measured value increases as hematocrit content (cellular fraction) is increased from 0.1-0.9 ³⁻⁵. Thus in the absence of cellular content, plasma is expected to have a yield stress of $\tau_Y \leq 10^{-4}$ Pa. The interfacial yield stress from our oscillatory strain sweep measurements $\tau_{sY} = G'_s \gamma_Y \approx 2.3 \times 10^{-4}$ Pa.m can be used to get a typical value for apparent yield stress, as $\tau_Y = l_G^{-1} \tau_{sY} \approx 3.9 \times 10^{-3}$ Pa, where we use the characteristic length scale $l_G = L$ for the DG geometry. This yield stress value obtained for BSA solutions is of the same order of magnitude as the yield stress of human blood (which reportedly has a larger yield stress than bovine blood ⁴), thus re-emphasizing how interfacial effects can produce systematic errors in viscosity

measurements if interfacial effects are not accounted for. It must be noted that even though serum albumins and blood samples from different species have qualitatively similar behavior, the absolute values of yield stress and viscosity of blood vary from one species to another. Again, for completeness we must note that blood plasma, as well as many of the biofluids contain other proteins, surfactants and/or biomolecules that will also affect the delicate interplay between the interfacial and the bulk rheological response⁶⁻⁸.

We note in the main text of the paper that the non-linearity induced by the sub-phase flow can be neglected for the interfacial viscosity measurements described in this study. We checked for the possible effect of non-linearity using the MATLAB script from Vandebril et al¹ (kindly provided by Jan Vermant), and confirmed that no correction was needed for these measurements on BSA solutions, as is shown by the overlap between the ‘raw’ or measured data and the corrected data shown in figure SI.8.

To conclude, in the context of our study on the BSA, the apparent yield stress arises from the formation of an interfacial film and, in the absence of a solution-air interface, no shear thinning will be observed for our protein solutions in the concentration range used in the current study. Yet, by measuring the two contributions from the sub-phase and interface independently using the VROC (microfluidic rheometer) and DWR geometry (attached to the ARG2, a stress-controlled torsional rheometer) respectively, we can provide an estimate for the apparent bulk viscosity response that will be measured for any viscometric flow geometry with a free interface that is mounted on a torsional rheometer. Similar yielding phenomenon, due to interfacial effects, can arise in bulk viscosity measurements involving other protein-rich biofluids, and we reiterate our hope that our methodology can provide a standard basis for deconvolving interfacial effects.

References

1. S. Vandebril, A. Franck, G. G. Fuller, P. Moldenaers and J. Vermant, *Rheol. Acta*, 2010, **49**, 131-144.
2. H. A. Barnes, *Journal of Non-Newtonian Fluid Mechanics*, 1999, **81**, 133-178.
3. C. Picart, J. M. Piau and H. Galliard, *Journal of Rheology*, 1998, **42**, 1-12.
4. S. E. Charm and G. S. Kurkland, *Blood flow and microcirculation*, John Wiley & Sons, New York, 1974.
5. E. W. Merrill, *Physiol. Rev.*, 1969, **49**, 863-888.
6. R. Miller and L. Liggieri, eds., *Interfacial rheology*, Brill, Leiden, 2009.
7. R. Miller, J. K. Ferri, A. Javadi, J. Kragel, N. Mucic and R. Wustneck, *Colloid and Polymer Science*, 2010, **288**, 937-950.
8. E. Dickinson, *Colloids and Surfaces B-Biointerfaces*, 1999, **15**, 161-176.

CAPTIONS:

Figure SI.1: Pressure data from microfluidic chip rheometer (mVROC – Type A05) (a) Comparison of the pressure measured by the each sensor as a function of sensor location, shown for 50 mg/ml BSA solution. (b) Pressure drop as a function of flow rate, for different concentrations of BSA.

Figure SI.2: Comparison of the bulk viscosity measured as function of shear rate as measured by separate VROC devices in two laboratories: Non-Newtonian Fluids research group at MIT, and Rheosense Inc. San Ramon, CA.

Figure SI.3: (a) Schematic of Double Wall Ring (DWR) fixture for interfacial rheometry (after (25)). The applied stress and resulting displacement are controlled and measured using a standard ARG2 controlled stress rheometer. In the present case, $R_1 = 31$ mm, $R_2 = 34.5$ mm, $R_3 = 35.5$ mm, $R_4 = 39.5$ mm and $H = 10$ mm. The ring has a square cross section, with width of 1 mm and is made out of platinum. **(b)** Interfacial storage (filled symbols) and loss modulus (hollow symbols) for different concentrations of BSA, measured as a function of strain amplitude at a fixed oscillation frequency $\omega = 1$ rad/s (using DWR fixture). The moduli increase monotonically with concentration. The downturn in the curves beyond $\gamma_y \approx 0.01$ represent the onset of yield.

Figure SI.4 Mastercurve of reduced interfacial stress as a function of reduced shear strain for different concentrations of BSA, shifted to a reference concentration of 50 mg/ml. The plateau-like region at high strains shows that the material yields plastically beyond a certain critical strain. The asymptotic slope of -1 corresponds to a yielding interface with a yield stress τ_{sY} and an apparent viscosity $\eta_s(\dot{\gamma}) = \tau_{sY} / \dot{\gamma}$.

Figure SI.5 Schematic of double gap Couette geometry. The interfacial region, represented in blue, is not drawn to the scale. The concentration gradient between the adsorbed, viscoelastic interfacial layer and the liquid subphase is also shown schematically.

Figure SI.6 Comparison of measured interfacial viscosity, η_s (DWR) (stars) with the values extracted using equation (SI.9) (see text for details). The plots of measured bulk viscosity (DG or CP, ARG2) compared with computed viscosity show that the simple model (equation SI.3 (DG) and SI.5 (CP) or SI.6-SI.7, see text) captures the contribution of interfacial effects.

Figure SI.7 Values of the shear-rate-dependent Boussinesq numbers of the different geometries for a 100 mg/ml BSA solution as a function of shear rate. The different length scales of the geometries (DG = double gap Couette, CP = cone-and-plate, DWR=double wall ring) lead to different values of Bo_s .

Figure SI.8 Comparison of the measured and corrected interfacial viscosity data; the correction is calculated using a MATLAB code following the approach outlined by Vandebril et al¹.

FIGURES:

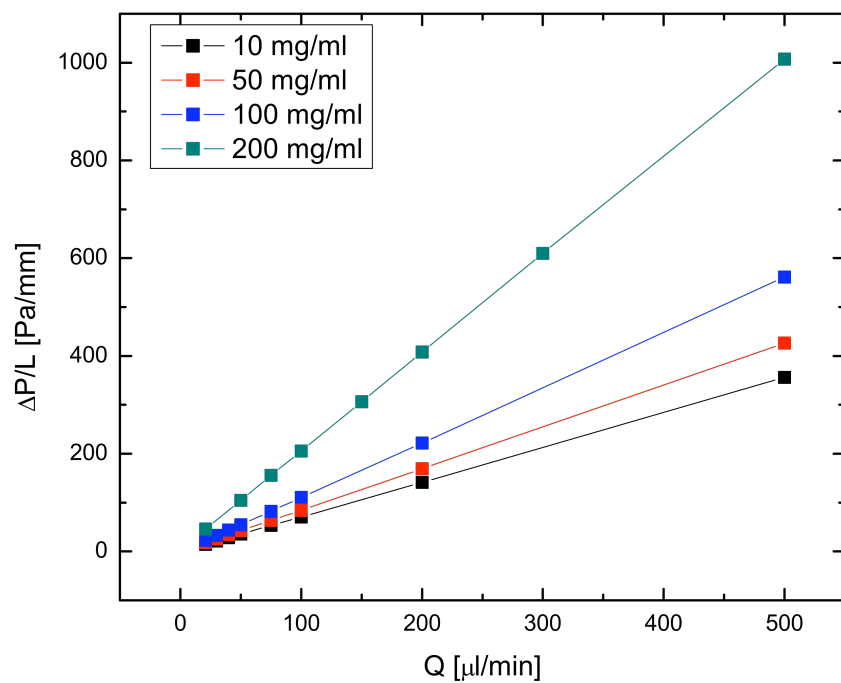
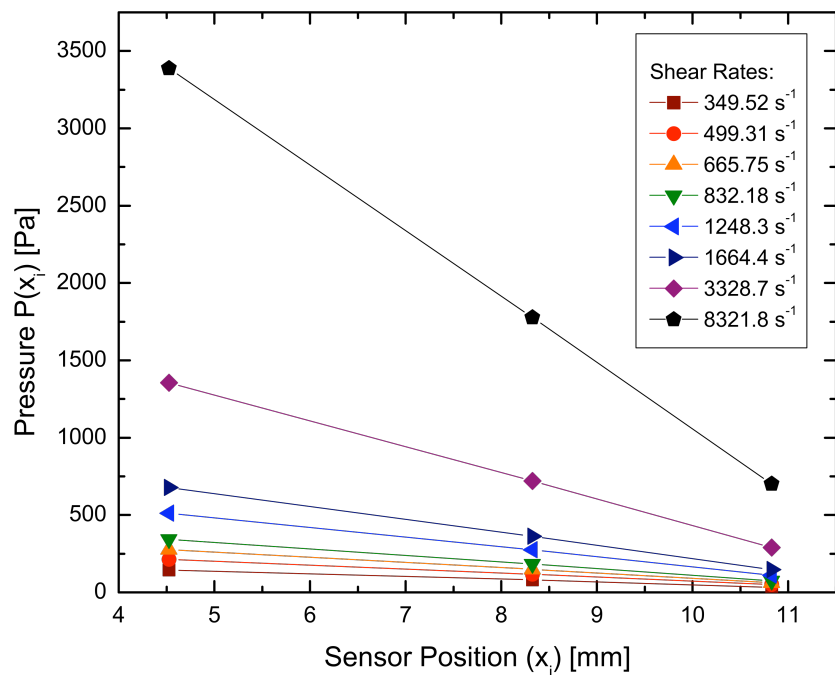


Figure SI.1

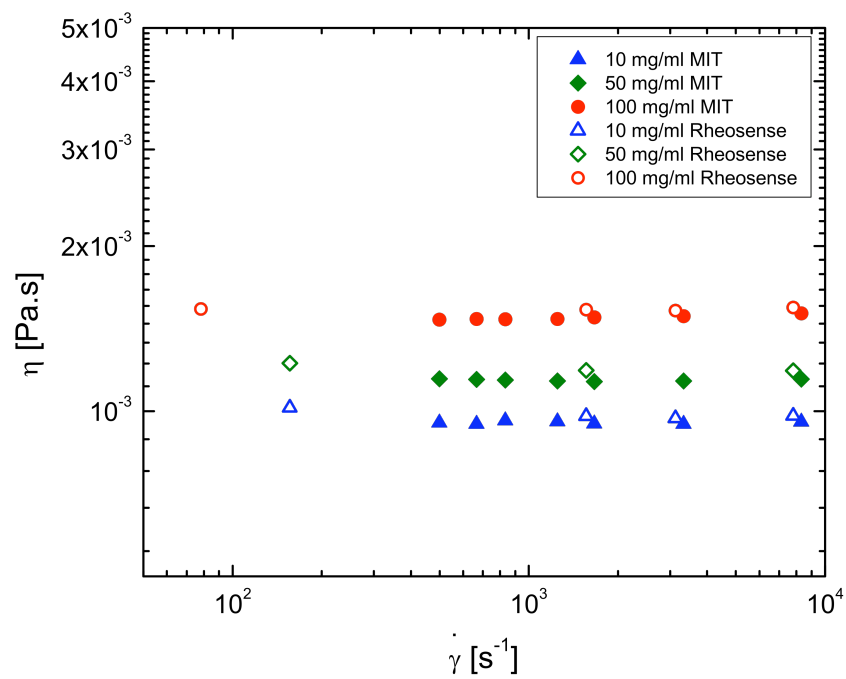


Figure SI.2

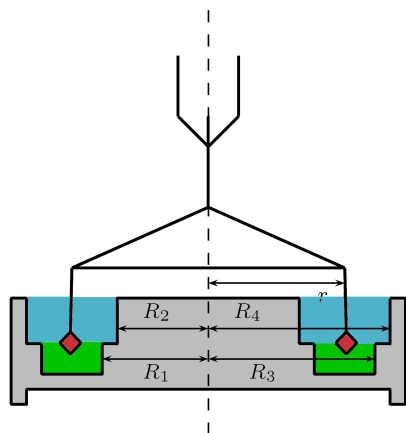


Figure SI.3 (a)

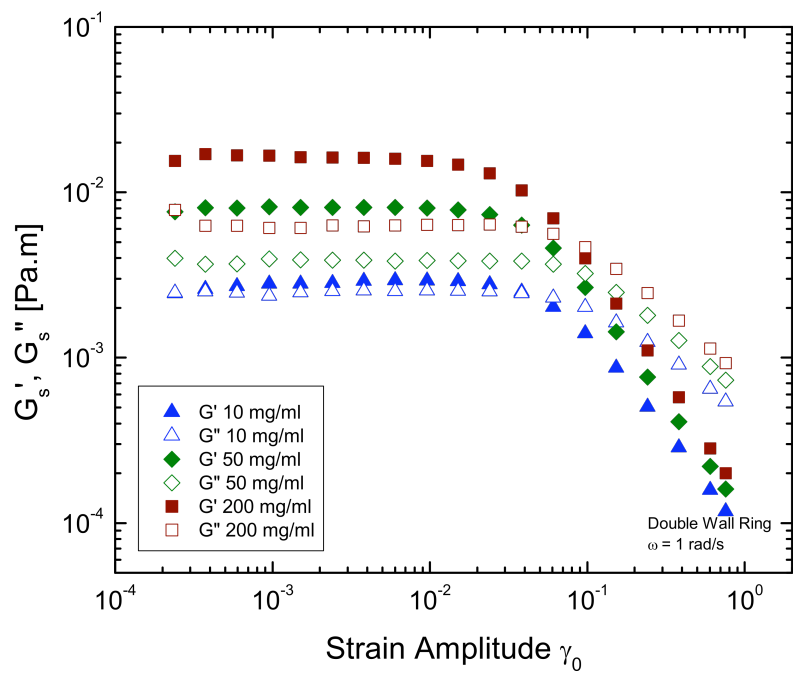


Figure SI.3 (b)

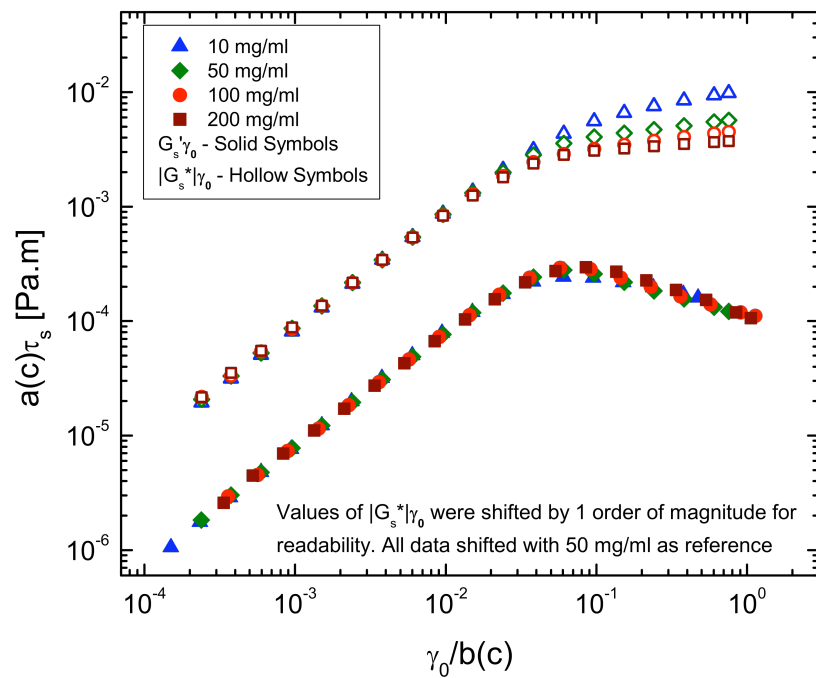


Figure SI.4

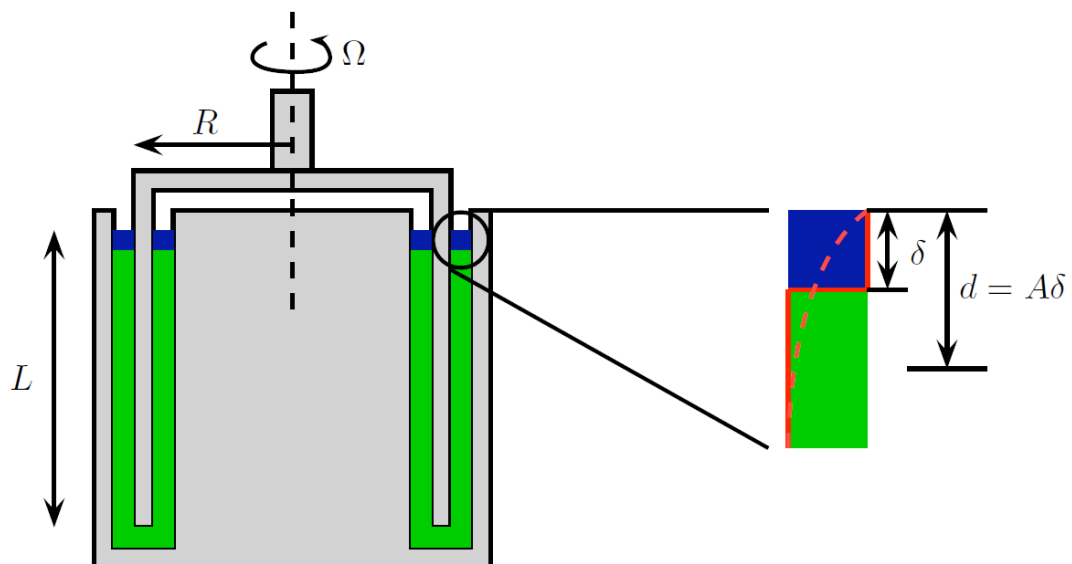


Figure SI.5

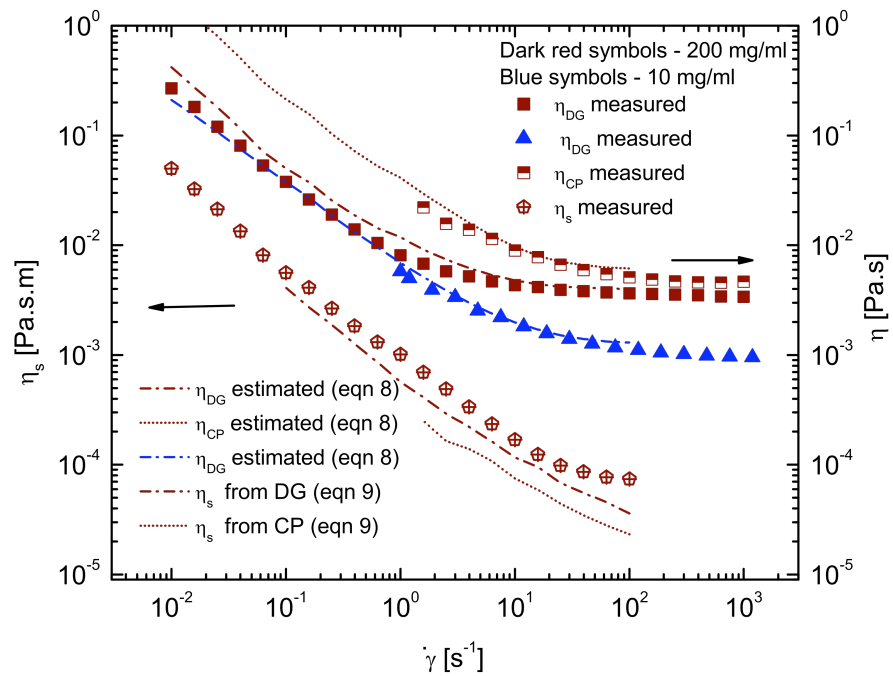


Figure SI.6

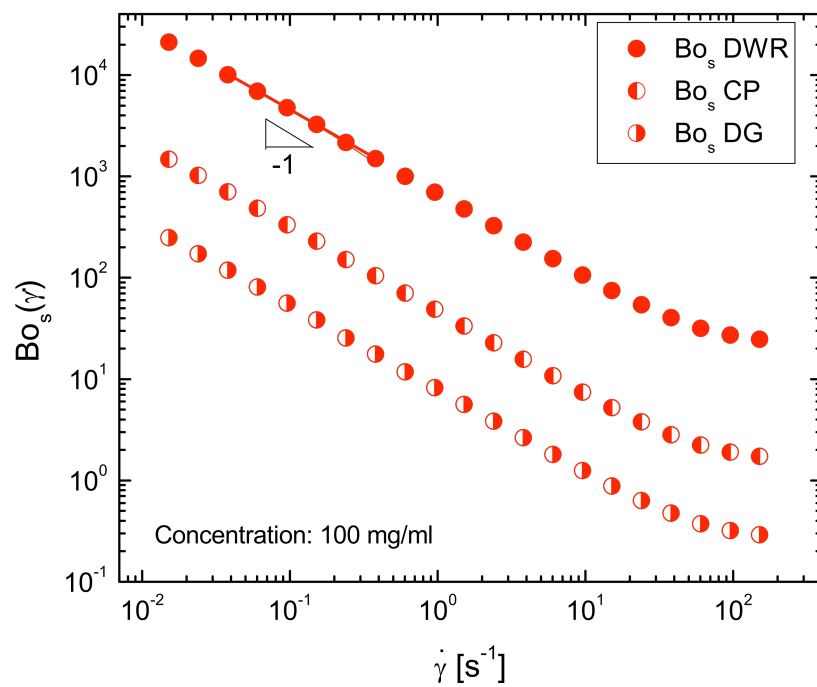


Figure SI.7

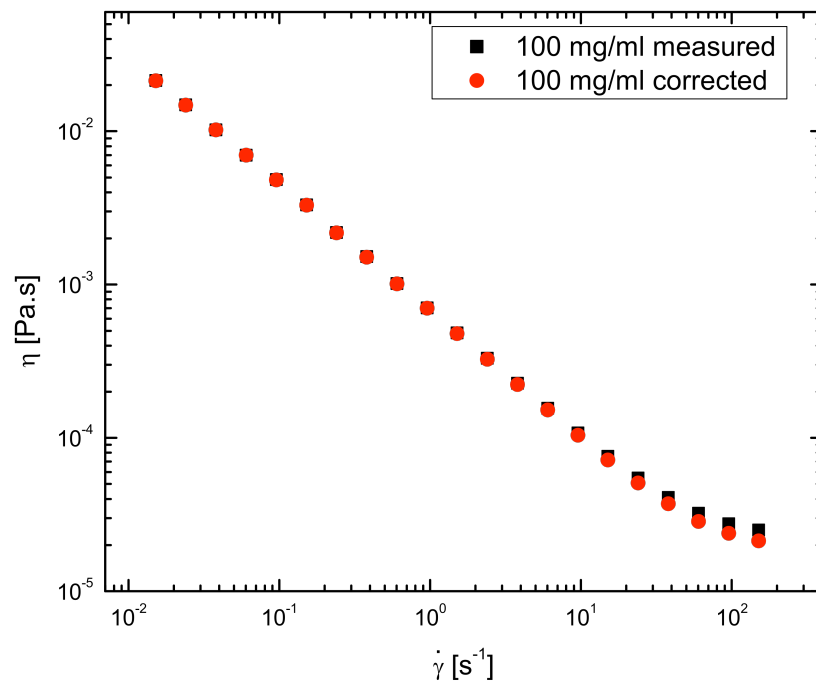


Figure SI.8